STAT3-mediated astrocyte reactivity associated with brain metastasis contributes to neurovascular dysfunction

Manuel Sarmiento Soto[1,7,8], James R. Larkin[1], Chris Martin[1,2], Alexandre A. Khrapitchev[1], Melissa Maczka[1,3], Vasiliki Economopoulos[1], Helen Scott[1], Carole Escartin[4,5], Gilles Bonvento[4,5], Sébastien Serres[1,6]*† and Nicola R. Sibson[1]*†

[1]Cancer Research UK and Medical Research Council Oxford Institute for Radiation Oncology, Department of Oncology, University of Oxford, Churchill Hospital, Oxford, UK.

[2]Department of Psychology, University of Sheffield, Western Bank, Sheffield, UK.

[3]Department of Statistics, 1 South Parks Road, Oxford, UK.

[4]Commissariat à l'Energie Atomique et aux Energies Alternatives, Département de la Recherche Fondamentale, Institut de Biologie François Jacob, MIRCen, F-92260 Fontenay-aux-Roses, France.

[5]Centre National de la Recherche Scientifique, Université Paris-Sud, Université Paris-Saclay, UMR 9199, Neurodegenerative Disease Laboratory, F-92260 Fontenay-aux-Roses, France.

[6]School of Life Sciences, University of Nottingham, Nottingham, UK.

[7]Department of Biochemistry and Molecular Biology, University of Seville, Spain.

[8]Institute of Biomedicine of Seville (IBiS), Hospital Universitario Virgen del Rocio/CSIC/University of Seville, Seville, Spain.

*Joint senior authors †Joint corresponding authors:

Prof. Nicola R. Sibson - Tel: + 44 1865 225836 Fax: +44 1865 857127

E-mail: nicola.sibson@oncology.ox.ac.uk

Postal address: Oxford Institute for Radiation Oncology, Department of Oncology, University of Oxford, Radiobiology Research Institute, Churchill Hospital, Oxford OX3 7LE.

Ass. Prof. Sebastien Serres – Tel: +44 115 8230394

E-mail: sebastien.serres@nottingham.ac.uk

Postal address: School of Life Sciences, Room D47, The Medical School, Queen's Medical Centre, University of Nottingham, Nottingham NG7 2UH.

Running title: Reactive astrocytes disrupt cerebrovascular function

Keywords: Brain metastasis, astrocytes, neurovascular unit, cerebral blood flow, STAT3

Funding: This work was supported by Cancer Research UK (grant number C5255/A15935 to NRS), a Faculty of Medicine and Health Sciences Research fund from the University of Nottingham (to SS) and a Marie-Sklodowska Curie Action-IF (to MSS).

Conflict of interest: The authors declare that there is no conflict of interest

This manuscript has 4337 words, 6 figures and 2 tables. Abstract has 247 words.

Abstract

Astrocytes are thought to play a pivotal role in coupling neural activity and cerebral blood flow. It has been shown, however, that astrocytes undergo morphological changes in response to brain metastasis, switching to a reactive phenotype, which has the potential to significantly compromise cerebrovascular function and contribute to the neurological sequelae associated with brain metastasis. Given that signal transducer and activator of transcription 3 (STAT3) is a key regulator of astrocyte reactivity, the aim of this study was to determine the impact of STAT3-mediated astrocyte reactivity on neurovascular function in brain metastasis.

We used rat models of brain metastasis and ciliary neurotrophic factor (CNTF) to induce astrocyte reactivity. Multimodal imaging, electrophysiology and immunohistochemistry were performed to determine the relationship between reactive astrocytes and changes in the cerebrovascular response to electrical and physiological stimuli. Subsequently, the STAT3 pathway in astrocytes was inhibited with WP1066 to determine the role of STAT3-mediated astrocyte reactivity, specifically, in brain metastasis.

We observed that astrocyte reactivity associated with brain metastases impaired cerebrovascular responses to stimuli at both the cellular and functional level, and to disrupt astrocyte-endothelial interactions in both animal models and human brain metastasis samples. Inhibition of STAT3-mediated astrocyte reactivity in rats with brain metastases restored cerebrovascular function, as shown by *in vivo* imaging, and limited cerebrovascular changes associated with tumour growth.

Together, these findings suggest that inhibiting STAT3-mediated astrocyte reactivity may confer significant improvements in neurological outcome for patients with brain metastases and, potentially, could be tested in other brain tumours.

Significance

Astrocyte reactivity associated with brain metastasis compromises cerebrovascular function and disrupts astrocyte-endothelial communication. Selective targeting of STAT3-mediated astrocyte reactivity significantly ameliorates this cerebrovascular dysfunction.

Introduction

Neurovascular coupling matches local cerebral blood flow (CBF) to neuronal energy use and, thus, ensures normal functioning of the brain(1). Whilst neuronal, astrocyte and pericyte mediated pathways have been implicated in neurovascular coupling to varying degrees(2), the significant contribution of astrocytes remains the most widely recognised(1-3).

Astrocyte processes cover most of the cerebrovascular surface and connect neurons with blood vessels(3-5), playing essential roles in recycling ions and neurotransmitters(3), supplying energy substrates to neurons(6), maintaining endothelial tight junctions to support the blood–brain barrier (BBB)(7), and releasing vasoactive molecules that regulate vascular tone(1). However, in response to disease or injury, astrocytes become reactive, displaying hypertrophy, upregulation of intermediate filament proteins (e.g. GFAP)(8) and metabolic changes(9). The consequences of this astrocyte reactivity, however, on the control of CBF remains unknown(3).

Changes in astrocyte function may be particularly pertinent in brain metastasis, where tumour cells interact closely with blood vessels. Such perivascular growth enables tumour cells to use the brain's vasculature for nutrient supply(10-13), but also disrupts astrocyte-vascular coupling and BBB integrity(12). At the same time, brain metastases trigger astrocyte reactivity from the earliest stages(10-13), and gradually expel astrocyte end-feet to the border of the tumour(14). Notably, signal transducer and activator of transcription 3 (STAT3) mediated astrocyte reactivity, specifically, has been shown to be important in maintaining the vascular co-option profile of brain metastases(15). Consequently, brain metastases may impact on cerebrovascular function not only through mechanical dissociation of astrocyte end-feet from vessels(12), but also through astrocyte reactivity *per se* and, as such, may contribute to the neurological sequelae associated with brain metastases. However, a lack of suitable animal models and

imaging techniques that are able to separate these two processes, to date, have limited our ability to fully understand their relative contributions.

The aim of this study, therefore, was to determine the impact of reactive astrocytes, specifically, on cerebrovascular function using animal models of brain metastasis and ciliary neurotrophic factor (CNTF) induced astrocyte reactivity(16,17), together with human brain metastasis biopsies. The CNTF model induces astrocyte reactivity, as observed in disease, in the absence of any other confounding pathology. Subsequently, the potential of inhibiting STAT3-mediated astrocyte reactivity to maintain vascular function was determined, as a potential adjuvant therapy for brain metastasis. Cortical vascular and neuronal function were measured using a multimodal imaging strategy involving magnetic resonance imaging (MRI), laser speckle contrast imaging (LSCI) and local field potential (LFP) measurements, in combination with post-mortem immunohistochemical analysis.

Materials and methods

All animal experiments were approved by the University of Oxford Clinical Medicine Ethics Review Committee and UK Home Office (Animals [Scientific Procedures] Act 1986), and conducted in accordance with the University of Oxford Policy on the Use of Animals in Scientific Research, the ARRIVE Guidelines and Guidelines for the Welfare and Use of Animals in Cancer Research(18). No overt clinical signs or weight loss were evident, in any cohort, over the experimental period. For *in vivo* experiments, blood gases were within the normal ranges for animals under isoflurane anaesthesia (Supplementary Table I). No effects of WP1066 treatment on blood gases and mean arterial blood pressure were observed (Supplementary Table I).

Metastatic tumour cell line, lentivirus and drug

For the brain metastasis model, an ENU1564 tumour cell line was used (kind gift from Professor G. Stoica, Texas A&M University), which originated from an N-ethyl-N-nitrosourea-induced mammary adenocarcinoma in a female Berlin-Druckrey IX (BD-IX) rat, and is highly metastatic to brain and bone tissues. As a rat cell line, there is no publicly available short tandem repeat (STR) profile for the cells, thus they have not been externally validated. Cells were tested for mycoplasma immediately prior to freezing each stock vial using MycoAlert kit (Lonza, UK). Stock vials were revived, grown for up to one week in DMEM supplemented with 10% FBS and 1% 200mM glutamine, harvested by trypsinisation, washed and then injected, as described previously(19).

For the reactive astrocyte model, lentivirus-mediated gene transfer of ciliary neurotrophic factor (CNTF-Lv) was used to induce sustained production of CNTF by neurons, which is released and then gives rise to stable activation of astrocytes via the STAT3 pathway, as described previously(9,16,17). To this end, self-inactivated lentiviruses encoding either the human CNTF gene or the (control) β-galactosidase gene (LacZ-Lv), under the control of the mouse phosphoglycerate kinase I promoter, were used (9,17). In the CNTF-Lv model, transfected neurons display a normal phenotype in terms of morphology, expression of neuronal proteins and spontaneous electrophysiological activity(9,17).

For STAT3 inhibition, a potent inhibitor that can cross the BBB, WP1066 (Millipore, UK) was injected intraperitoneal daily (3mg/kg) using dimethyl sulfoxide (DMSO) as a vehicle.

Experimental models

All experimental procedures used in this study were approved by the United Kingdom Home Office. Two cohorts of female BD-IX rats (Charles River, France), 6-12 weeks old, were injected intracortically in the whisker barrel somatosensory cortex. One cohort of rats was injected with either 10^3 metastatic ENU1564 cells in PBS (n=8) or PBS alone (n=6). The second cohort of rats was injected with either CNTF-Lv (n=9) or LacZ-Lv (n=7) diluted in PBS at a concentration of 100ng p24/µl. The third cohort of rats was injected with 10^3 metastatic ENU1564 cells (n=10). Animals injected with ENU1564 cells were randomly distributed for intraperitoneal injection of either 50µl WP1066 in DMSO (3mg/kg, n=5) or 50µl DMSO (n=5). All animals were transcardially perfusion-fixed under terminal anaesthesia at the end of the experiment for histological analysis. For full details please see Supplementary Methods.

Magnetic resonance imaging

All MRI experiments were performed on a horizontal bore 9.4T spectrometer driven by an Agilent DirectDrive™ console (Agilent Technologies, Santa Clara, CA, USA). Animals were anaesthetised with 1-2% isoflurane in 70%N_2/30%O_2 and positioned in a 72mm quadrature volume transmit coil with 4 channels phased array surface receiver (RAPID Biomedical GmbH, Rimpar, Germany). In some animals, a cannula was positioned in the tail vein prior to the MRI experiment for gadolinium-DTPA (Gd-DTPA) injection to identify potential blood-brain barrier breakdown.

Multimodal acquisitions included T_1- and T_2-weighted MRI and arterial spin labelling (ASL) MRI. For technical details please visit the Supplementary Methods section.

Laser Speckle Contrast Imaging (LSCI)

Through the cranial window, superficial (ascending venules and pial vessels) and deep blood vessels (penetrating arterioles and capillary beds) within the cortex were visible (0.5-1mm deep). Animals underwent LSCI on the day following MRI measurements. For full details regarding LSCI set up and surgery see Supplementary data. (20,21).

Local Field Potentials (LFPs)

In a subset of animals, LFPs were recorded to measure neuronal responses to the same electrical stimulation of the whisker pad (see above). In this case, burr holes were drilled over both barrel cortices and an electrode (0.155mm diameter, Teflon insulated platinum; Bilaney Consultants Ltd., Sevenoaks, UK) inserted to a depth of 0.5mm under stereotaxic control, as described previously(22). Electrode signals were recorded using a CED 1902 isolated pre-amplifier and signal processor (Cambridge Electronic Design limited, Cambridge, UK), which was controlled using Spike2.7 data acquisition and analysis package software (Cambridge Electronic Design limited, Cambridge, UK). Electrode signals were acquired with a waveform sampling rate of 10 kHz, 2μs per time unit resolution and without notch filtering. Low frequency noise was eliminated from the electrode signal using a 50/60Hz noise eliminator (Hum Bug, Quest scientific, Vancouver, Canada).

MRI data analysis

Signal intensity on T_1 and T_2 weighted images in the ipsilateral and contralateral cortices of animals was quantified using ImageJ software package (NIH, Bethesda, MD, USA)(23). CBF maps were quantified with nonlinear perfusion signal modelling(24) using the BASIL (Bayesian Inference for Arterial Spin Labelling MRI) toolset in FSL version 5.0 (FMRIB

Software Library, Oxford, UK). For more details regarding data analysis please see Supplementary data (24).

LSCI data analysis

LSCI datasets were redefined and down-sampled to 1Hz for data analysis. To quantify the time-course of the CBF response after electrical stimuli, datasets were averaged over 10 trials and regions of interest (ROI) drawn around areas corresponding to the whisker barrel cortex. The CBF response and its associated time-series were extracted from the ROIs in both ipsilateral (left) and contralateral (right) whisker barrel cortices. More information regarding data acquisition can be found in Supplementary data.

LFP data analysis

At the end of the LFP recording period, waveform and sampling times were converted into a MATLAB file using Spike 2.7 software. The data were aligned with the stimulation time-series and binned at 100Hz. LFP responses to whisker pad stimulation were extracted from 0 to 16s after stimulus using in-house MATLAB scripts. To quantify neuronal response magnitudes, amplitude (mV) was calculated from the average response to the first pulse in the stimulation train (over a 50ms period following stimulation onset), as described previously(22).

Immunohistochemistry and immunofluorescence

All animals were transcardially perfusion-fixed under terminal anaesthesia with 0.9% heparinised saline followed by periodate lysine paraformaldehyde (PLP) containing only 0.025% glutaraldehyde (PLP_{light}) at the end of LSCI and LFP measurements. The brains were post-fixed, cryoprotected, embedded in tissue-tek (Sakura Finetek Europe, Zoeterwoude, The Netherlands) and frozen in isopentane at -40˚C. Frozen, 20µm thick, serial sections spanning

the somatosensory cortex were cut from fixed tissue and mounted on gelatin-coated glass slides. Immunohistochemistry was performed with antibodies against markers of activated astrocytes (1:300, GFAP, Dako, Ely, UK), STAT3 (1:300, STAT3α, Cell Signaling Technology), neurons (1:500, NeuN, Millipore, Abingdon, UK), blood vessels (1:100, CD31, Abcam, Cambridge, UK), microglia (1:200, OX42 [cd11b/c], Abcam, Cambridge, UK), cyclooxygenase-1 and 2 (1:100, COX-1/2) (Abcam, Cambridge, UK), inducible isoform of nitric oxide synthetase (1:50, iNOS, Abcam Cambridge, UK), nitrotyrosine (1:400, NT, Millipore, Abingdon, UK), alpha-smooth muscle actin (1:100, α-SMA; Abcam Cambridge, UK), β-dystroglycan (1:200, Abcam, Cambridge, UK), Claudin-5 (1:200, Abcam, Cambridge, UK) and cytochrome p450-4A (1:100, Abcam Cambridge, UK), the enzyme responsible for the biosynthesis of 20-hydroxyeicosatetraenoic acid (20-HETE).

Immunofluorescent microscopy was performed to identify reactive astrocytes (GFAP), microglia (OX42), neurons (NeuN), blood vessels (CD31), cyclooxygenase-1 and 2 (COX-1/2), inducible isoform of nitric oxide synthase (iNOS), cytochrome p450-4A, α-SMA and β-dystroglycan and Claudin-5. More details about the performed protocols can be found in Supplementary Methods.

Immunohistochemistry and immunofluorescence analysis

Photomicrographs of each brain section were obtained by scanning each section with Aperio® Image Analysis (Leica, Germany), or using a Nikon Microscope (Nikon E800, Japan) coupled to a RoHS camera (RoHS, UK). Subsequently, images were analysed using ImageScope (Leica, Germany) and Qcapture Pro software (Qimaging, UK), respectively.

Immunofluorescent images were acquired using an inverted confocal microscope (LSM-710, Carl Zeiss Microimaging, Jena, Germany) or Leica DM IRBE (Leica, Germany). Detection

ranges were set to eliminate crosstalk between fluorophores: 409-485nm for AMCA, 494-553nm for Alexa Fluo 488 and 561-595nm for Cy3/Texas Red. Images were analysed using in ImageJ software package (NIH)(23). For full information regarding the colocalisation studies please see Supplementary data.

Statistical analysis

All data are given as mean ± SEM. Statistical analysis was performed using GraphPad Prism (GraphPad Software, Inc., La Jolla, CA, USA). Unpaired or paired *t*-tests were used to compare data between ipsi- and contralateral cortices. Unpaired *t*-tests were used to identify differences between DMSO and WP1066 groups. The relationships between ASL-CBF maps and areas of reactive astrocytes were tested by a bivariate correlation analysis, including calculation of the Pearson's correlation coefficient (*r*).

Results

Perivascular growth of focally-induced brain metastases

One week after intracortical injection of ENU1564 cells, 94% of all brain metastases were associated with blood vessels (Figure 1(a-c); $p<0.001$ compared to non-associated), indicating that focally-induced metastases were predominantly perivascular. Of the blood vessels associated with ENU1564 cells, the majority (74%) were capillaries or small veins (<8.5μm diameter(25); Figure 1d), rather than arterioles, arteries and large veins (>8.5μm (25); $p<0.001$ small *vs.* large).

Neurovascular coupling is disrupted in areas of brain metastasis

LSCI measurement of CBF responses to electrical stimulation of the whisker pad *in vivo*, revealed a focal region of hyperaemia in the contralateral (normal) cortex during stimulation, but a considerably reduced response in the ipsilateral (metastasis bearing) cortex of ENU1564-injected animals (Figure 1e). Quantitatively, the CBF response was significantly reduced in the ipsilateral *vs.* contralateral cortex (~50%; Figure 1f; $p<0.05$). Simultaneous LFP recordings of neuronal responses showed no significant differences between ipsi- and contralateral cortices (Figure 1g). No significant differences between ipsi- and contralateral cortices were seen in PBS-injected animals for either CBF or LFP responses (Supplementary Figure S1(a-c)). Immunohistochemically, no differences in the number of NeuN-positive neurons between cortices in either group (excluding metastatic foci) were evident (Supplementary Figure S1d). Together, these findings suggest that neurovascular coupling is disrupted in the presence of brain metastases.

Brain metastases alter BBB-astrocyte morphology and induce reactive astrocytes

Within the metastatic foci, astrocyte end-feet appeared to be displaced from blood vessels owing to the perivascular growth pattern of the metastatic cells (mean displacement = 31.3±2.4μm; Figure 1h (i)). At the same time, a widespread area of reactive astrocytes was evident around the metastatic foci in the ipsilateral cortex (Figure 1h (ii), dotted line, 0.54±0.11mm^2). Moreover, a significant decrease in co-localisation between β-dystroglycan, GFAP and CD31 was evident throughout the area of reactive astrocytes in ENU1564 animals (Figure 1i, Table I; $p<0.05$), suggesting detachment of astrocyte end-feet from the vascular endothelium unrelated to the direct mechanical effects of the metastatic cells. No decrease in co-localisation was observed in PBS-injected animals (Figure 1i, Table I).

Despite the apparent dissociation of astrocyte end-feet from the vasculature, BBB integrity remained intact, as determined by post-Gd-DTPA T_1-weighted MRI (Supplementary Figure S1e) and immunohistochemical detection of Claudin-5, a key tight junctional protein in BBB paracellular permeability (Supplementary Figure S1f-g). Moreover, although blood vessels associated with metastatic cells were abnormal in appearance (Supplementary Figure S1h), no change in blood vessel number was evident in either metastatic foci or areas of reactive astrocytes (Supplementary Figure S1i).

CNTF-induced reactive astrocytes

To assess the effect of reactive astrocytes *per se* on neurovascular function, we used a model of CNTF-induced reactive astrocytes(17) (Figure 2a). Six weeks after intracortical injection, an area of reactive astrocytes was observed in CNTF-Lv animals (Figure 2b; 0.46±0.09 mm^2), whilst negligible astrocyte reactivity was observed in control LacZ-Lv animals (Figure 2b). Reactive astrocytes induced by CNTF-Lv did not alter BBB integrity, as determined by post-Gd-DTPA T_1-weighted MRI (Figure 2c) and Claudin-5/CD31 (vessel marker) co-localization (Supplementary Figure S2a), neuronal number (Supplementary Figure S2b) or blood vessel numbers (Supplementary Figure S2c).

Neurovascular coupling is disrupted in areas of reactive astrocytes

LSCI measurements in CNTF-Lv injected animals indicated a significant reduction in the amplitude of the CBF response to whisker barrel stimulation in the ipsilateral cortex (~70%) compared to the contralateral cortex (Figure 2(d-e); $p<0.01$). No significant difference was observed in control LacZ-Lv injected animals (Supplementary Figure S2(d-e)). As for the metastasis model, LFP responses to electrical stimulation were unaltered in both groups of

animals (Figure 2f, Supplementary Figure S2f), supporting the concept that neurovascular coupling is disrupted when astrocytes become reactive.

Reactive astrocytes alter BBB-astrocyte morphology

Again, a significant decrease in co-localisation of β-dystroglycan, GFAP and CD31 was observed (Figure 2g, Table I; $p<0.05$), which was not seen in LacZ-Lv animals (Figure 2g, Table I). When assessing co-localisation of β-dystroglycan and GFAP alone, no change was found in either ENU1546 or CNTF-Lv models (Table I), indicating that reactive astrocytes exhibit reduced adhesion to the vascular endothelium rather than reduced expression of β-dystroglycan *per se*.

Inhibition of STAT3 reduces astrocyte reactivity in response to brain metastasis

Animals injected with ENU1564 cells and treated with WP1066 (Figure 3a), a selective inhibitor of the JAK/STAT3 pathway mediating astrocyte reactivity(15), showed a significant decrease in the area of astrocyte reactivity compared to vehicle (DMSO)-treated animals for both GFAP (~55%; Figure 3b-c; $p<0.05$) and STAT3 staining (~77%; Figure 3b-c; $p<0.05$). However, no significant reduction was evident in the area of metastatic foci (0.63 ± 0.12 *vs.* $0.55\pm0.27 mm^2$; Figure 3c). In WP1066-treated animals, nuclear STAT3 expression in reactive astrocytes was decreased compared to DMSO-treated animals (Fig 3b).

Inhibition of STAT3 in reactive astrocytes improves cerebrovascular function

As expected, (*cf.* Figure 1f), DMSO-treated ENU1564 animals, showed a significantly reduced (~48%) CBF response to electrical stimulation in the metastasis-bearing cortex compared to

the contralateral cortex (Figure 3d; $p<0.05$). In contrast, WP1066-treated ENU1564 animals showed a much smaller and non-significant reduction (~26%) in CBF response compared to the contralateral hemisphere (Figure 3f). As above, LFP responses to whisker pad stimulation were unaltered in both groups (Figure 3(e-g)).

Subsequently, we demonstrated that cerebrovascular responses to hypercapnia(26) were significantly reduced in both ENU1564 (~44%) and CNTF-Lv (~40%) models, but not in their respective control groups (PBS and LacZ-Lv; Supplementary Figure S3; $p<0.001$ and $p<0.05$, respectively). Again, STAT3-inhibition improved the hypercapnia-evoked vascular responses in ENU1564-injected animals, with no significant difference evident between cortices (Supplementary S3).

Together these findings indicate that inhibition of STAT3-mediated astrocyte reactivity can, at least partially, reverse cerebrovascular dysfunction associated with brain metastases.

Reactive astrocytes reduce basal cerebral blood flow

Measurements of basal CBF using ASL-MRI showed a significant reduction compared to the contralateral cortex of animals injected with either ENU1564 cells or CNTF-Lv (Figure 4(a-d), $p<0.01$). Notably, the area of reactive astrocytes as a percentage of the somatosensory cortex was much larger than the metastatic foci (40% *vs.* 3%, respectively), and correlated spatially with the region of reduced CBF for both ENU1564 and CNTF-Lv models (Figure 4e; $p<0.05$; Pearson's coefficient correlation $r^2=0.33$). In contrast, no changes in basal CBF were observed in PBS or LacZ-Lv control groups (Figure 4(f-g)).

STAT3 inhibition with WP1066 largely reversed the reduction in basal CBF observed in ENU1564 animals (Figure 4(h-i)), with a significant difference compared to DMSO-treated

animals ($p<0.05$). Given that the area of reactive astrocytes showed a much greater reduction after WP1066 treatment (~55%) than the metastatic foci (~12%), we suggest that reactive astrocytes, rather than the presence of metastases *per se*, underlie the reduced basal CBF in metastasis-bearing animals.

STAT3-mediated reactive astrocytes regulate vessel diameter and vasoactive pathways

Large vessels (>8.5μm) showed significant vasoconstriction in the area of reactive astrocytes within the ipsilateral *vs.* contralateral cortex, in both ENU1564 and CNTF-Lv models (Figure 5(a-b); $p<0.05$). Moreover, co-localisation between cytochrome p450-4A, an endothelium-dependent vasoconstrictor(27,28), and α-smooth muscle actin (αSMA), a marker of smooth muscle cells on large blood vessels(29), was significantly greater in ipsilateral *vs.* contralateral cortex for both models (Figure 5(c-d), Table II; $p<0.05$). No differences were evident in control animals (Figure 5(c-d), Table II). No changes in cytochrome p450-4A levels were observed in either astrocytes or microglia (Figure 5(e-f)).

In contrast, a significant increase in the diameters of smaller vessels (<8.5μm diameter) in the region of astrocyte reactivity was evident in both ENU1564 and CNTF-Lv animals (Figure 5(g-h)), compared to controls (PBS and LacZ-Lv; Figure5(g-h); $p<0.001$). Co-localisation of the vasodilatory molecule iNOS with astrocytes was significantly greater in ENU1564 and CNTF-Lv animals compared to controls (Figure 5i; $p<0.05$ and $p<0.01$; respectively), together with increased cortical levels of nitrotyrosine (NT), a marker of nitric oxide(30) (Figure 5j). Similarly, astrocytic levels of COX-1, a key enzyme in the arachidonic acid vasodilatory pathway(1), were significantly greater in ipsilateral *vs.* contralateral cortex of ENU1564 and CNTF-Lv groups (Figure 5k; $p<0.05$ and $p<0.01$, respectively), but not in controls (PBS and LacZ-Lv; Figure 5k). COX-1 showed greater co-localisation with astrocytes than any other

cells (Supplementary Table II), suggesting they are the dominant cell population driving COX-1-mediated vasodilation, whilst both astrocytes and endothelial cells showed the highest levels of iNOS co-localisation. A significantly higher number of OX42-positive pixels was found in the ENU1564 group compared to PBS, CNTF-Lv or LacZ-Lv injected groups (Supplementary Table III), confirming an inflammatory microglia/macrophages response in presence of brain metastases(31,32), but no contribution of microglia/macrophages in the CNTF-Lv model(9,17).

No changes were observed in the levels of COX-2 in astrocytes, iNOS in endothelial cells, or iNOS/COX-1 in microglia in any of the groups (Supplementary Figure S4), suggesting that vasodilation of small vessels reflects activation of the nitric oxide and arachidonic acid pathways primarily in astrocytes. A significant decrease in both iNOS/GFAP and COX1/GFAP co-localisation was evident in WP1066- *vs.* DMSO-treated ENU1564 animals (Figure 5l). However, neither iNOS nor COX-1 was altered in microglia, endothelial cells or smooth muscle cells following WP1066 treatment (Supplementary Figure S5). Additionally, expression of iNOS and COX-1 was not altered in microglia (OX42) in the ipsilateral cortices of ENU1564 animals treated with WP1006 (Supplementary Figures S6). These results indicate that STAT3 inhibition is primarily limited to reactive astrocytes within the metastatic microenvironment.

Reactive astrocytes are associated with vasoactive pathways in human brain metastasis

Reactive astrocytes were evident in human brain metastasis biopsies (Oxford Brain Bank: OBB-SH-1088-2013-) primarily in the areas surrounding tumour colonies (Figure 6a). As in the animal models, co-localisation between cytochrome p450-4A and αSMA staining was seen on blood vessels associated with brain metastases (Figure 6b), and both iNOS and COX-1

staining were present in astrocytes (Figure 6(c-d)). The percentage of αSMA- and cytochrome p450-4A-positive blood vessels was greater around metastatic foci compared to control brain (Table II). Significantly greater levels of both iNOS and COX-1 per GFAP-positive pixel, and cytochrome p450-4A per αSMA-positive pixel, were found in the area of reactive astrocytes around metastatic foci compared to non-tumour tissues (Figure 6e; $p<0.001$ and $p<0.05$, respectively).

Discussion

In a rat model of brain metastasis, we have demonstrated impairment of cerebrovascular function, disruption of astrocyte-vascular connections and widespread reactive astrocytes. Studies using a model of CNTF-induced astrocyte reactivity, indicated that reactive astrocytes *per se* can compromise cerebrovascular function, whilst inhibition of STAT3-mediated astrocyte reactivity partially reversed the cerebrovascular dysfunction associated with brain metastases. These findings suggest that STAT3-mediated astrocyte reactivity in brain metastasis may contribute to cerebrovascular, and hence neurological, dysfunction in patients.

In glioma, tumour cells displace astrocyte end-feet from blood vessels enabling tumour growth in the perivascular space(12,33). Similarly, we and others have shown that brain metastases grow in this co-optive fashion, particularly during the micrometastastic stages(10,11,34). Here, we show that not only are astrocytes displaced from the vasculature mechanically, but that reactive astrocytes distant from the metastatic foci dissociate from the vasculature. Watkins *et al*.(12) hypothesised that displacement of astrocytes from the vasculature by invading glioma cells prevents vasoactive molecules from reaching endothelial cells, thus disrupting neurovascular coupling(12). Although this may also be partly the case in brain metastasis, our

findings suggest that widespread reactive astrocytes, outwith the spatially restricted metastatic foci, contribute significantly to disruption of vascular function. Critically, a similar compromise of cerebrovascular function was observed in the CNTF-Lv model, in which astrocytes were activated to a reactive phenotype for a prolonged period, whilst neuronal activity was preserved(17). Similarly, CBF responses to hypercapnia were compromised in both models. To date, only two studies have suggested that vasoactive pathways in astrocytes are involved in CBF responses to hypercapnia(35,36). Our data support this concept and suggest that astrocyte reactivity may compromise autoregulation.

One possible explanation for the reduced CBF responses to both neuronal activation and hypercapnia is that vasodilation across the vascular bed leads to reduced vascular reserve(37,38). However, although we found vasodilation in the microvascular network, the arteriolar vessels appeared to be constricted and basal blood flow was reduced, in keeping with restricted arteriolar flow. Moreover, we found more cytochrome p450-4A, the enzyme responsible for the biosynthesis of vasoconstrictor 20-HETE(27,28), on smooth muscle cells at the arterioles. Consequently, we speculate that suppression of CBF responses to stimuli in the presence of reactive astrocytes may reflect either basal upregulation of vasoconstrictory pathways in the arteriolar bed and/or upregulation of enzymes that mediate vasodilation (iNOS and COX-1) downstream of the arterioles and reduced vascular reserve within the microvascular bed. A recent study has suggested that astrocytes regulate CBF at the capillary and arteriole levels through two distinct mechanisms(39), reinforcing the concept that reactive astrocytes exert differential effects on arterioles and capillaries.

Importantly, upregulation of the above vasoactive mediators was mirrored in all human brain metastasis samples studied, typically at the leading edge of the tumour. Recent studies have identified the JAK/STAT3 pathway in reactive astrocytes as a novel target for neurological

diseases(40), brain metastasis(41) and glioblastoma(42). Together with significant anti-tumor effects(15), data suggest that inhibition of STAT3 may also reduce the immunosuppressive environment of brain tumours induced by cross-talk between astrocytes and microglia (15,43), implicating this inflammatory microenvironment as a potential target for treatment in brain metastasis(44). Given our data showing that STAT3 inhibition restores impaired cerebrovascular function in brain metastasis, we propose that therapy suppressing astrocyte reactivity may also be effective in reducing metastasis-associated neurocognitive effects and in improving the response of current therapies that are limited by tumour-associated hypoxia and abnormal vasculature (45,46). Notably, reduced blood flow has been linked to the neurological symptoms associated with brain metastases, such as seizures(47-49) and stroke(50), and this could be investigated in ongoing brain tumour clinical trials with STAT3 inhibitors (e.g. NCT01904123).

With regards to limitations of the current study, although we have shown that reactive astrocytes are the dominant cell type producing prostaglandin mediated vasodilation via COX-1 activity, NO-mediated vasodilation is not solely driven by reactive astrocytes. Thus, separating the contributions of different stromal cell populations to the production of vasoactive mediators requires further investigation, potentially using genetically encoded calcium indicators, transgenic techniques or viral constructs, in combination with *in vivo* recording of haemodynamic response. Additionally, only one brain metastasis model was used in this study. Given that ENU model is well-established(19,51-53), rather than using a second brain metastasis model we considered it to be more relevant to use a model of CNTF-induced reactive astrocytes in order to determine the effect of reactive astrocytes specifically, in the absence of metastases, on neurovascular function. At the same time, the immunohistochemical data obtained from human brain metastasis samples lend further support to our experimental findings. Finally, we did not fully suppress astrocyte reactivity in our models via STAT3

inhibition, suggesting that astrocyte activation may be complex and heterogeneous(54). For example, the NFκB (nuclear factor kappa-light-chain-enhancer of activated B cells) signalling pathway has been shown to contribute to the neurotoxicity of a subpopulation of reactive astrocytes induced by activated neuroinflammatory microglia(55) and, thus, may be an important additional pathway of astrocyte activation in brain metastasis that warrants further investigation.

In summary, this study is the first empirical demonstration that STAT3-mediated astrocyte reactivity associated with brain metastasis contributes to acute cerebrovascular dysfunction. STAT3 inhibition may, therefore, limit detrimental neurological symptoms associated with disease progression and improve outcome for patients with brain metastases.

Acknowledgement:

The authors thank Dr James Meakin for assistance with implementation of the pCASL sequence and Professor G. Stoica (Texas A&M University) for the ENU1564 cells.

References:

1. Attwell D, Buchan AM, Charpak S, Lauritzen M, Macvicar BA, Newman EA. Glial and neuronal control of brain blood flow. Nature **2010**;468:232-43
2. Howarth C. The contribution of astrocytes to the regulation of cerebral blood flow. Front Neurosci **2014**;8:103
3. Iadecola C, Nedergaard M. Glial regulation of the cerebral microvasculature. Nat Neurosci **2007**;10:1369-76
4. Mathiisen TM, Lehre KP, Danbolt NC, Ottersen OP. The perivascular astroglial sheath provides a complete covering of the brain microvessels: an electron microscopic 3D reconstruction. Glia **2010**;58:1094-103
5. Kacem K, Lacombe P, Seylaz J, Bonvento G. Structural organization of the perivascular astrocyte endfeet and their relationship with the endothelial glucose transporter: a confocal microscopy study. Glia **1998**;23:1-10
6. Pellerin L, Bouzier-Sore AK, Aubert A, Serres S, Merle M, Costalat R*, et al.* Activity-dependent regulation of energy metabolism by astrocytes: an update. Glia **2007**;55:1251-62
7. Abbott NJ, Ronnback L, Hansson E. Astrocyte-endothelial interactions at the blood-brain barrier. Nat Rev Neurosci **2006**;7:41-53
8. Sofroniew MV, Vinters HV. Astrocytes: biology and pathology. Acta Neuropathol **2010**;119:7-35
9. Escartin C, Pierre K, Colin A, Brouillet E, Delzescaux T, Guillermier M*, et al.* Activation of astrocytes by CNTF induces metabolic plasticity and increases resistance to metabolic insults. J Neurosci **2007**;27:7094-104
10. Carbonell WS, Ansorge O, Sibson N, Muschel R. The vascular basement membrane as "soil" in brain metastasis. PLoS One **2009**;4:e5857
11. Serres S, Soto MS, Hamilton A, McAteer MA, Carbonell WS, Robson MD*, et al.* Molecular MRI enables early and sensitive detection of brain metastases. Proc Natl Acad Sci U S A **2012**;109:6674-9
12. Watkins S, Robel S, Kimbrough IF, Robert SM, Ellis-Davies G, Sontheimer H. Disruption of astrocyte-vascular coupling and the blood-brain barrier by invading glioma cells. Nat Commun **2014**;5:4196
13. Kienast Y, von Baumgarten L, Fuhrmann M, Klinkert WE, Goldbrunner R, Herms J*, et al.* Real-time imaging reveals the single steps of brain metastasis formation. Nat Med **2010**;16:116-22
14. Hasko J, Fazakas C, Molnar K, Meszaros A, Patai R, Szabo G*, et al.* Response of the neurovascular unit to brain metastatic breast cancer cells. Acta Neuropathol Commun **2019**;7:133
15. Priego N, Zhu L, Monteiro C, Mulders M, Wasilewski D, Bindeman W*, et al.* STAT3 labels a subpopulation of reactive astrocytes required for brain metastasis. Nat Med **2018**;24:1024-35
16. Lisovoski F, Akli S, Peltekian E, Vigne E, Haase G, Perricaudet M*, et al.* Phenotypic alteration of astrocytes induced by ciliary neurotrophic factor in the intact adult brain, As revealed by adenovirus-mediated gene transfer. J Neurosci **1997**;17:7228-36
17. Escartin C, Brouillet E, Gubellini P, Trioulier Y, Jacquard C, Smadja C*, et al.* Ciliary neurotrophic factor activates astrocytes, redistributes their glutamate transporters GLAST and GLT-1 to raft microdomains, and improves glutamate handling in vivo. J Neurosci **2006**;26:5978-89
18. Workman P, Aboagye EO, Balkwill F, Balmain A, Bruder G, Chaplin DJ*, et al.* Guidelines for the welfare and use of animals in cancer research. Br J Cancer **2010**;102:1555-77
19. Serres S, Martin CJ, Sarmiento Soto M, Bristow C, O'Brien ER, Connell JJ*, et al.* Structural and functional effects of metastases in rat brain determined by multimodal MRI. Int J Cancer **2014**;134:885-96
20. Boas DA, Dunn AK. Laser speckle contrast imaging in biomedical optics. J Biomed Opt **2010**;15:011109

21. Ayata C, Dunn AK, Gursoy OY, Huang Z, Boas DA, Moskowitz MA. Laser speckle flowmetry for the study of cerebrovascular physiology in normal and ischemic mouse cortex. J Cereb Blood Flow Metab **2004**;24:744-55
22. Spain A, Howarth C, Khrapitchev AA, Sharp T, Sibson NR, Martin C. Neurovascular and neuroimaging effects of the hallucinogenic serotonin receptor agonist psilocin in the rat brain. Neuropharmacology **2015**;99:210-20
23. Schneider CA, Rasband WS, Eliceiri KW. NIH Image to ImageJ: 25 years of image analysis. Nature methods **2012**;9:671-5
24. Groves AR, Chappell MA, Woolrich MW. Combined spatial and non-spatial prior for inference on MRI time-series. NeuroImage **2009**;45:795-809
25. Francois-Dainville E, Buchweitz E, Weiss HR. Effect of hypoxia on percent of arteriolar and capillary beds perfused in the rat brain. J Appl Physiol (1985) **1986**;60:280-8
26. Xu HL, Koenig HM, Ye S, Feinstein DL, Pelligrino DA. Influence of the glia limitans on pial arteriolar relaxation in the rat. American journal of physiology Heart and circulatory physiology **2004**;287:H331-9
27. Guo AM, Janic B, Sheng J, Falck JR, Roman RJ, Edwards PA*, et al.* The cytochrome P450 4A/F-20-hydroxyeicosatetraenoic acid system: a regulator of endothelial precursor cells derived from human umbilical cord blood. J Pharmacol Exp Ther **2011**;338:421-9
28. Escalante B, Omata K, Sessa W, Lee SG, Falck JR, Schwartzman ML. 20-hydroxyeicosatetraenoic acid is an endothelium-dependent vasoconstrictor in rabbit arteries. Eur J Pharmacol **1993**;235:1-7
29. Rensen SS, Doevendans PA, van Eys GJ. Regulation and characteristics of vascular smooth muscle cell phenotypic diversity. Neth Heart J **2007**;15:100-8
30. Franze T, Weller MG, Niessner R, Poschl U. Comparison of nitrotyrosine antibodies and development of immunoassays for the detection of nitrated proteins. Analyst **2004**;129:589-96
31. Andreou KE, Soto MS, Allen D, Economopoulos V, de Bernardi A, Larkin JR*, et al.* Anti-inflammatory Microglia/Macrophages As a Potential Therapeutic Target in Brain Metastasis. Front Oncol **2017**;7:251
32. O'Brien ER, Kersemans V, Tredwell M, Checa B, Serres S, Soto MS*, et al.* Glial activation in the early stages of brain metastasis: TSPO as a diagnostic biomarker. J Nucl Med **2014**;55:275-80
33. Holash J, Maisonpierre PC, Compton D, Boland P, Alexander CR, Zagzag D*, et al.* Vessel cooption, regression, and growth in tumors mediated by angiopoietins and VEGF. Science **1999**;284:1994-8
34. Winkler F, Kienast Y, Fuhrmann M, Von Baumgarten L, Burgold S, Mitteregger G*, et al.* Imaging glioma cell invasion in vivo reveals mechanisms of dissemination and peritumoral angiogenesis. Glia **2009**;57:1306-15
35. Niwa K, Haensel C, Ross ME, Iadecola C. Cyclooxygenase-1 participates in selected vasodilator responses of the cerebral circulation. Circ Res **2001**;88:600-8
36. Howarth C, Sutherland B, Choi HB, Martin C, Lind BL, Khennouf L*, et al.* A Critical Role for Astrocytes in Hypercapnic Vasodilation in Brain. J Neurosci **2017**;37:2403-14
37. Austin VC, Blamire AM, Allers KA, Sharp T, Styles P, Matthews PM*, et al.* Confounding effects of anesthesia on functional activation in rodent brain: a study of halothane and alpha-chloralose anesthesia. Neuroimage **2005**;24:92-100
38. Sicard K, Shen Q, Brevard ME, Sullivan R, Ferris CF, King JA*, et al.* Regional cerebral blood flow and BOLD responses in conscious and anesthetized rats under basal and hypercapnic conditions: implications for functional MRI studies. Journal of cerebral blood flow and metabolism : official journal of the International Society of Cerebral Blood Flow and Metabolism **2003**;23:472-81

39. Mishra A, Reynolds JP, Chen Y, Gourine AV, Rusakov DA, Attwell D. Astrocytes mediate neurovascular signaling to capillary pericytes but not to arterioles. Nat Neurosci **2016**;19:1619-27
40. Ben Haim L, Carrillo-de Sauvage MA, Ceyzeriat K, Escartin C. Elusive roles for reactive astrocytes in neurodegenerative diseases. Front Cell Neurosci **2015**;9:278
41. Priego N, Zhu L, Monteiro C, Mulders M, Wasilewski D, Bindeman W*, et al.* STAT3 labels a subpopulation of reactive astrocytes required for brain metastasis. Nat Med **2018**;24:1024-35
42. Heiland DH, Gaebelein A, Borries M, Worner J, Pompe N, Franco P*, et al.* Microenvironment-Derived Regulation of HIF Signaling Drives Transcriptional Heterogeneity in Glioblastoma Multiforme. Mol Cancer Res **2018**;16:655-68
43. Henrik Heiland D, Ravi VM, Behringer SP, Frenking JH, Wurm J, Joseph K*, et al.* Tumor-associated reactive astrocytes aid the evolution of immunosuppressive environment in glioblastoma. Nat Commun **2019**;10:2541
44. Berghoff AS, Preusser M. The inflammatory microenvironment in brain metastases: potential treatment target? Chin Clin Oncol **2015**;4:21
45. Berghoff AS, Ilhan-Mutlu A, Dinhof C, Magerle M, Hackl M, Widhalm G*, et al.* Differential role of angiogenesis and tumour cell proliferation in brain metastases according to primary tumour type: analysis of 639 cases. Neuropathol Appl Neurobiol **2015**;41:e41-55
46. Berghoff AS, Breckwoldt MO, Riedemann L, Karimian-Jazi K, Loew S, Schlieter F*, et al.* Bevacizumab-based treatment as salvage therapy in patients with recurrent symptomatic brain metastases. Neurooncol Adv **2020**;2:vdaa038
47. Weil RJ, Palmieri DC, Bronder JL, Stark AM, Steeg PS. Breast cancer metastasis to the central nervous system. Am J Pathol **2005**;167:913-20
48. Crivellari D, Pagani O, Veronesi A, Lombardi D, Nole F, Thurlimann B*, et al.* High incidence of central nervous system involvement in patients with metastatic or locally advanced breast cancer treated with epirubicin and docetaxel. Ann Oncol **2001**;12:353-6
49. Bendell JC, Domchek SM, Burstein HJ, Harris L, Younger J, Kuter I*, et al.* Central nervous system metastases in women who receive trastuzumab-based therapy for metastatic breast carcinoma. Cancer **2003**;97:2972-7
50. Dardiotis E, Aloizou AM, Markoula S, Siokas V, Tsarouhas K, Tzanakakis G*, et al.* Cancer-associated stroke: Pathophysiology, detection and management (Review). Int J Oncol **2019**;54:779-96
51. Ray KJ, Simard MA, Larkin JR, Coates J, Kinchesh P, Smart SC*, et al.* Tumor pH and Protein Concentration Contribute to the Signal of Amide Proton Transfer Magnetic Resonance Imaging. Cancer Res **2019**;79:1343-52
52. Miller JJ, Grist JT, Serres S, Larkin JR, Lau AZ, Ray K*, et al.* (13)C Pyruvate Transport Across the Blood-Brain Barrier in Preclinical Hyperpolarised MRI. Sci Rep **2018**;8:15082
53. Larkin JR, Simard MA, de Bernardi A, Johanssen VA, Perez-Balderas F, Sibson NR. Improving Delineation of True Tumor Volume With Multimodal MRI in a Rat Model of Brain Metastasis. Int J Radiat Oncol Biol Phys **2020**;106:1028-38
54. Liddelow SA, Barres BA. Reactive Astrocytes: Production, Function, and Therapeutic Potential. Immunity **2017**;46:957-67
55. Liddelow SA, Guttenplan KA, Clarke LE, Bennett FC, Bohlen CJ, Schirmer L*, et al.* Neurotoxic reactive astrocytes are induced by activated microglia. Nature **2017**;541:481-7

Tables:

% colocalization	CD31/ βDG		GFAP/ βDG		GFAP/CD31	
	ipsi	contra	ipsi	contra	ipsi	contra
ENU cells	13±2*	23±4	71±2	72±2	40±7	46±3
PBS	29±2	32±3	41±5	47±6	41±6	37±4
Lv-CNTF	18±3**	40±5	66±9	51±4	45±2*	57±3
Lv-LacZ	42±5	45±3	44±5	34±10	35±5	31±3

Table I: Percentage co-localisation of CD31, GFAP and β-dystroglycan staining in ipsilateral (ipsi) and contralateral (contra) cortices of animals injected with either ENU1564 cells (top; N=7) or PBS (bottom; N=3); 4 sections per animal; paired *t*-test; mean ± SEM; *$p<0.05$,**$p<0.01$.

(+) p450-4A vessels	% of (+) αSMA vessels (n)	% of (-) SMA vessels (n)
ENU cells	72±3 (51)	28±3 (20)
PBS	43±10 (26)	57±10 (28)
Lv-CNTF	79±4 (39)	21±4 (11)
Lv-LacZ	48±5 (24)	52±5 (26)
Human brain metastasis	73±2 (51)	27±2 (18)

Table II: Percentage of cytochrome p450-4A-positive blood vessels that are either αSMA positive or negative for all groups of animals. All data are given as mean ± SEM, with number of blood vessels counted (n).

Figure 1. Brain metastasis growth disrupts both neurovascular coupling and astrocyte-blood vessel interaction. (a) Schematic of the experimental design. **(b)** Photomicrograph showing immunohistochemical detection of blood vessels (CD31, brown) in a rat injected with 10^3 ENU1564 cells (arrows), in both cortices (ipsilateral and contralateral). **(c)** Graph showing percentage of metastatic ENU1564 cells attached to the vasculature as quantified by presence of CD31 staining within a metastasis. N=4 animals; unpaired *t*-test (mean± SEM; ***p<0.001). **(d)** Graph showing classification of vessels in the tumour area according to the 8.5µm diameter threshold in animals injected with ENU-1564 cells (N=4 animals; 4 sections per animals; unpaired *t*-test; mean± SEM; ***p<0.001). **(e)** Laser speckle contrast images showing cortical blood flow in an animal injected with ENU1564 cells before and during whisker-barrel stimulation (*injection site; anterior-to-posterior (A) and rostral-to-caudal (R) axes). **(f)** Graphs showing CBF response and ΔCBF amplitude (arbitrary unit [a.u]; see online methods) in both cortices of ENU1564-injected animals (N=8; mean ± SEM; paired *t*-test, *p<0.05). **(g)** Graphs showing local field potential (LFP) responses and LFP amplitude (mV; see online methods) to whisker-barrel stimulation in both cortices of ENU1564-injected animals (N=6; mean ± SEM). **(h)** Representative immunofluorescence images showing dissociation of astrocyte end-feet from blood vessels co-opted by perivascular metastases (arrows in (i)), and at lower magnification changes in cellular morphology of astrocytes in the area associated with brain metastases (within dotted line in (ii)). **(i)** Immunofluorescence images taken from ipsilateral and contralateral cortices of animals injected with either ENU1564 cells or PBS and showing astrocytes (GFAP, blue), blood vessels (CD31, red) and β-dystroglycan (βDG, green). To assess the interaction of astrocytes with blood vessels, quantitation of red and blue pixels within the green channel was measured in both cortices. Graphs showing percentage co-localisation of CD31, GFAP and β-dystroglycan staining both sides of animals injected with either ENU1564 cells (top; N=7) or PBS (bottom; N=3); 4 sections per animal; paired *t*-test; mean ±

SEM; *p<0.05. Ipsilateral and injected cortex represented by (I) and contralateral (C) cortex used as control.

Figure 2. Reactive astrocytes disrupt both neurovascular coupling and astrocyte-blood vessel interaction. (a) Schematic of the experimental design. **(b)** Photomicrographs showing immunohistochemical detection of reactive astrocytes (GFAP; brown) in the ipsilateral cortex of animals injected with either CNTF-Lv **(**left**)** or the control LacZ-Lv **(**right**)**. **(c)** T_2- and gadolinium-enhanced T_1 weighted magnetic resonance images showing that BBB integrity remained intact in the cortex of animals injected with CNTF-Lv at 6 weeks post-injection. Graph shows signal intensity in the cortices (paired *t*-test; mean ± SEM, n=3). Box indicates region of reactive astrocytes. **(d)** Laser speckle contrast images showing cortical blood flow in an animal injected with CNTF-Lv pre- and post- stimulation of the whisker-barrel (*injection site; anterior-posterior (A) and rostral-to-caudal (R) axes). **(e)** Graphs showing CBF responses and ΔCBF amplitudes (arbitrary unit [a.u]; see online methods) to whisker-barrel stimulation in cortices of CNTF-Lv-injected animals (N=8; mean ± SEM; paired t-test; **p<0.01). **(f)** Graphs showing LFP responses and LFP amplitudes (mV; see online methods) to whisker-barrel stimulation in both sides of CNTF-Lv-injected animals (N=7; mean ± SEM). **(g)** Immunofluorescence images of animals injected with either CNTF-Lv or the control LacZ-Lv showing astrocytes (GFAP, blue, AMCA), blood vessels (CD31, red, Texas Red) and β-dystroglycan (β-DG, green, A488). Graphs show percentage co-localisation of CD31, GFAP and β-dystroglycan staining of animals injected with either CNTF (top; N=7) or control LacZ-Lv (bottom; N=4); (4 sections per animal; paired *t*-test; mean ± SEM; *p<0.05). Ipsilateral/injected cortex represented by (I) and contralateral (C) cortex used as control.

Figure 3. Inhibition of STAT3 in reactive astrocytes improves cerebrovascular function. **(a)** Schematic of the experimental design. **(b)** Photomicrographs showing immunohistochemical detection of GFAP (top panel) and STAT3 (bottom panel) positive cells (brown) in the ipsilateral cortices (dotted line) of ENU1564-animals treated with DMSO (control) or WP1066 (STAT3 inhibitor). Arrows show STAT3. **(c)** Graphs showing area of GFAP (top left panel; n=5), STAT3 (bottom left panel; n=5) and tumour cells (right panel) in ipsilateral cortices. Unpaired *t*-test (mean± SEM; *p<0.05). **(d)** Laser speckle contrast images showing cortical blood flow in an ENU1564-animal treated with DMSO (control) before and during whisker-barrel stimulation (top panel; *injection site; anterior-posterior (A) and rostro-caudal (R) axes). Graphs showing CBF response and ΔCBF amplitude (arbitrary unit [a.u]; see online methods) in animals treated with DMSO (control) (bottom panel; N=4; mean ± SEM; paired *t*-test, *p<0.05). **(e)** Graphs showing local field potential (LFP) responses and LFP amplitude (mV; see online methods) to whisker-barrel stimulation in animals treated with DMSO (control) (N=3; mean ± SEM). **(f)** Laser speckle contrast images showing cortical blood flow in animals treated with WP1066 before and during whisker-barrel stimulation (top panel; *injection site; anterior-posterior (A) and rostro-caudal (R) axes). Graphs showing CBF response and ΔCBF amplitude (arbitrary unit [a.u]; see online methods) in animals treated with WP1066 (bottom panel; N=4; mean ± SEM). **(g)** Graphs showing local field potential (LFP) responses and LFP amplitude (mV; see online methods) to whisker-barrel stimulation in animals treated with WP1066 (bottom panel; N=4; mean ± SEM). For all graphs, cortices of ENU1564-animals are referred as ipsilateral (I) and contralateral (C).

Figure 4. Reactive astrocytes are associated with changes in vasoactive pathways. (a) Immunofluorescence images showing co-localisation (arrows) of cytochrome p450-4A-positive cells (green), αSMA-positive cells (red) and nuclei (DAPI, blue) in CNTF-Lv-injected

animals. **(b)** Graphs showing percentage of co-localisation between cytochrome p450-4A and αSMA staining in ipsilateral (black bar) and contralateral (white bar) cortices of all four experimental groups. **(c)** Immunofluorescence images showing co-localisation of iNOS (green), astrocytes (GFAP, red) and nuclei (blue; DAPI) in both cortices of CNTF-Lv-injected animals. **(d)** Graph shows percentage co-localisation of iNOS and GFAP in ipsilateral (black bar) and contralateral (white bar) cortices of all experimental groups. **(e)** Immunofluorescence images showing co-localisation of COX-1(green), astrocytes (GFAP, red) and nuclei (blue; DAPI) in ipsilateral (black bar) and contralateral (white bar) cortices of CNTF-Lv-injected animals. **(f)** Graph shows percentage co-localisation of COX-1 and GFAP. All quantitative analysis performed using N=4 animals; 4 sections per animal, unless stated otherwise; mean ± SEM; paired *t*-test, *p<0.05, **p<0.01). **(g)** Graphs showing total number of iNOS/GFAP (left panel) and COX1/GFAP (right panel) positive pixels in the ipsilateral cortices of DMSO (control) or WP1066 experimental groups. N=4 animals; unpaired t-test (mean± SEM; **p<0.01). For all graphs, cortices of ENU1564-animals are referred as ipsilateral (I) and contralateral (C).

Figure 5. Reactive astrocytes are associated with changes in vasoactive pathways in human brain metastasis tissue. (a) Photomicrographs showing immunohistochemical detection of reactive astrocytes (GFAP; brown) surrounding brain metastases (*) in human tissue. **(b)** Immunofluorescence images showing co-localisation (*) of cytochrome p450-4A-positive cells (green), αSMA (red) and nuclei (blue; DAPI). **(c)** Immunofluorescence images showing co-localisation of iNOS (green), astrocytes (GFAP, red) and nuclei (blue; DAPI) in the blood vessels surrounding the tumour colonies. Insets (i) and (ii) with * indicates iNOS/GFAP co-localisation. **(d)** Immunofluorescence images showing co-localisation of COX-1 (green), astrocytes (GFAP, red) and nuclei (blue; DAPI). Insets (i) and (ii) with *

indicates COX-1/iNOS co-localisation. (e) Graph shows percentage co-localisation of iNOS and GFAP, COX-1/GFAP and p450/αSMA in intratumoral (I, black bar) and extratumoral (E, white bar) regions of human tissue (3 brains; 4 sections per brain; mean ± SEM; unpaired *t*-test, *p<0.05, ***p<0.001).

Figure 1

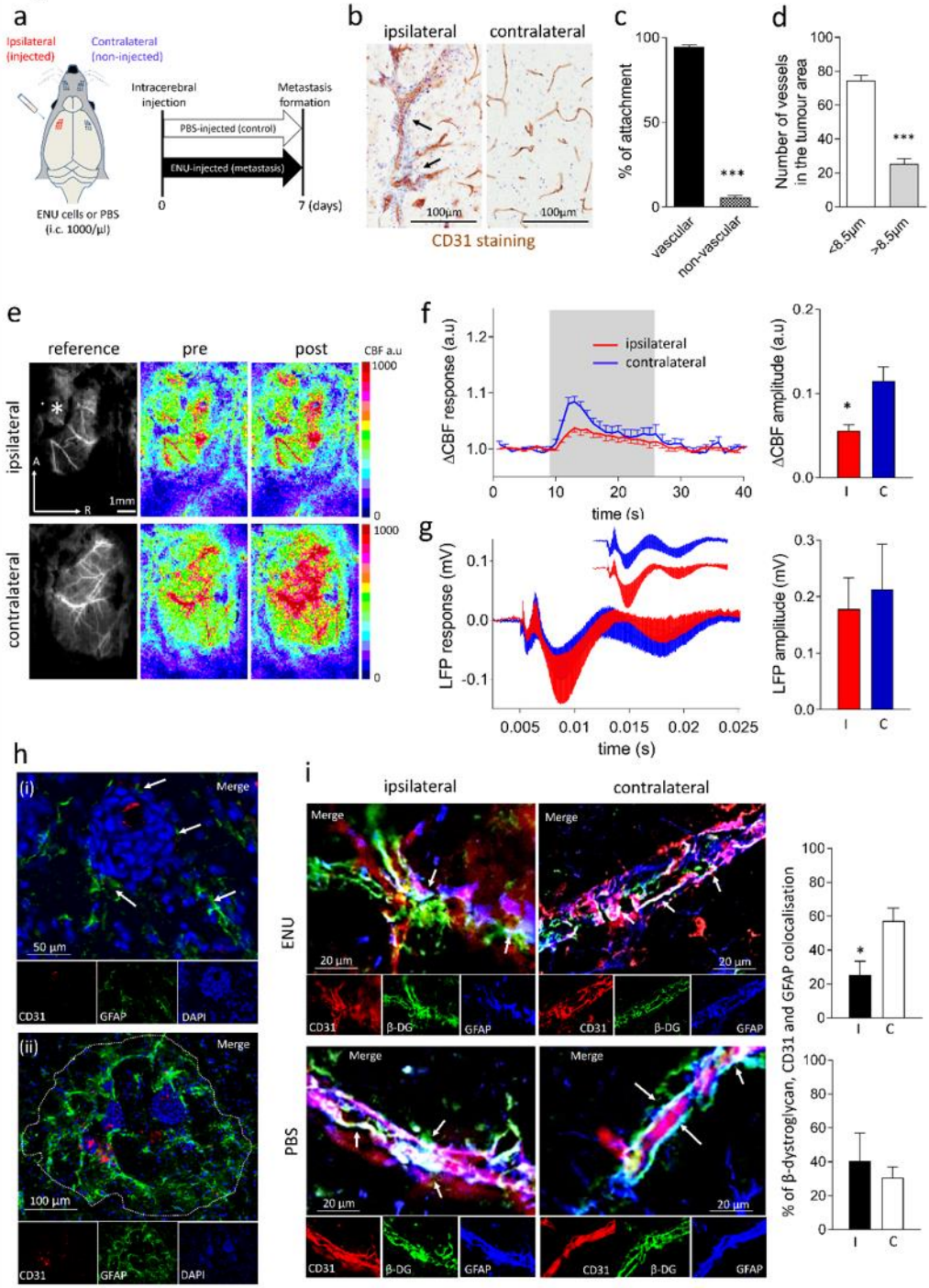
a
Ipsilateral (injected)
Contralateral (non-injected)
Intracerebral injection
Metastasis formation
PBS-injected (control)
ENU-injected (metastasis)
0
7 (days)
ENU cells or PBS (i.c. 1000/µl)
b
ipsilateral
contralateral
100µm
CD31 staining
c
% of attachment
vascular
non-vascular
d
Number of vessels in the tumour area
<8.5µm
>8.5µm
e
reference
pre
post
CBF a.u
ipsilateral
contralateral
1mm
f
ΔCBF response (a.u)
ipsilateral
contralateral
time (s)
ΔCBF amplitude (a.u)
g
LFP response (mV)
time (s)
LFP amplitude (mV)
h
(i)
Merge
50 µm
CD31
GFAP
DAPI
(ii)
100 µm
i
ipsilateral
contralateral
ENU
PBS
20 µm
β-DG
% of β-dystroglycan, CD31 and GFAP colocalisation

Figure 2

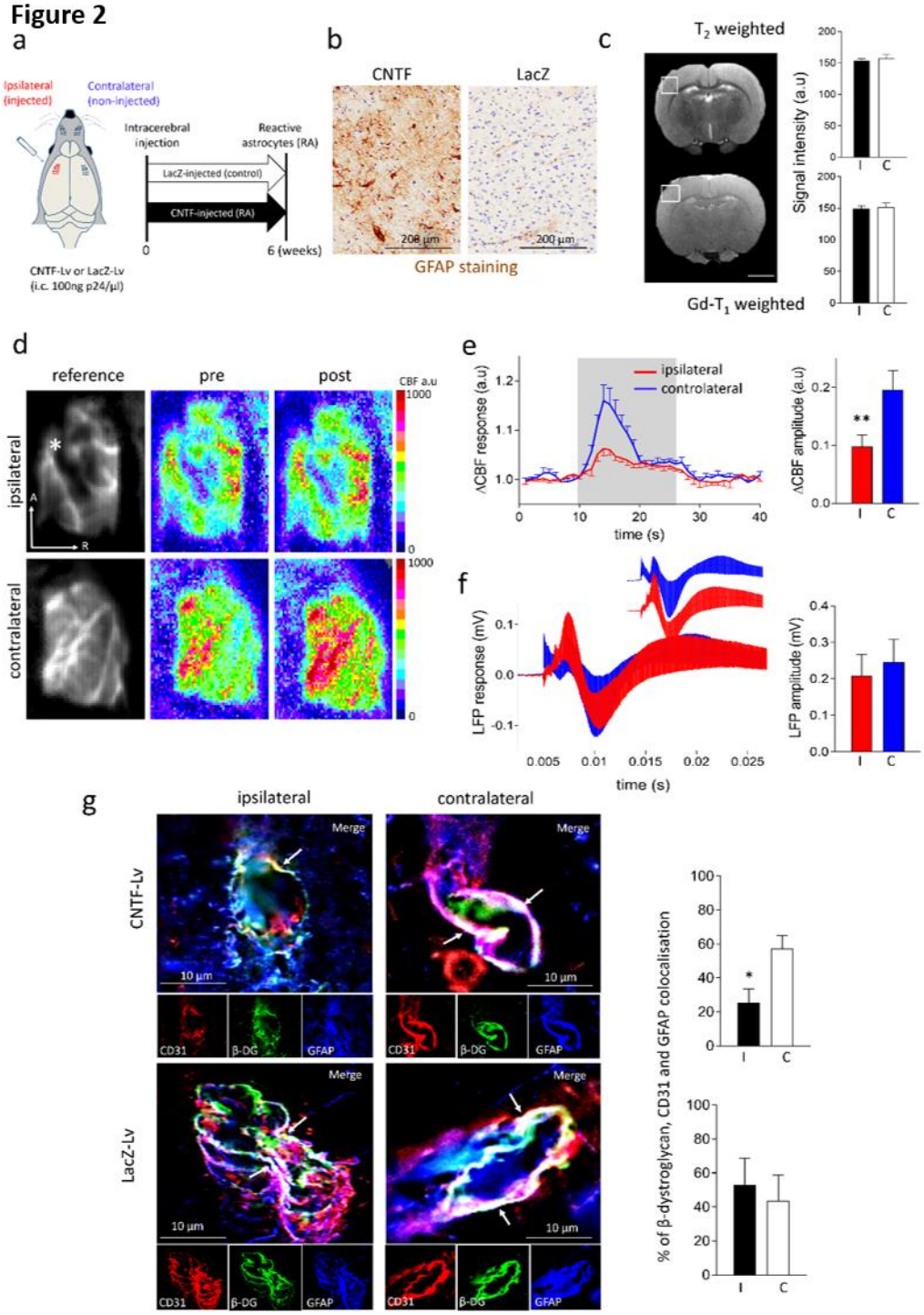
a
Ipsilateral (injected)
Contralateral (non-injected)
Intracerebral injection
Reactive astrocytes (RA)
LacZ-injected (control)
CNTF-injected (RA)
0
6 (weeks)
CNTF-Lv or LacZ-Lv (i.c. 100ng p24/µl)
b
CNTF
LacZ
208 µm
200 µm
GFAP staining
c
T2 weighted
Gd-T1 weighted
Signal intensity (a.u)
I
C
d
reference
pre
post
CBF a.u
1000
0
ipsilateral
contralateral
e
ipsilateral
controlateral
ΔCBF response (a.u)
time (s)
ΔCBF amplitude (a.u)
**
f
LFP response (mV)
time (s)
LFP amplitude (mV)
g
ipsilateral
contralateral
CNTF-Lv
LacZ-Lv
Merge
10 µm
CD31
β-DG
GFAP
% of β-dystroglycan, CD31 and GFAP colocalisation
*

Figure3

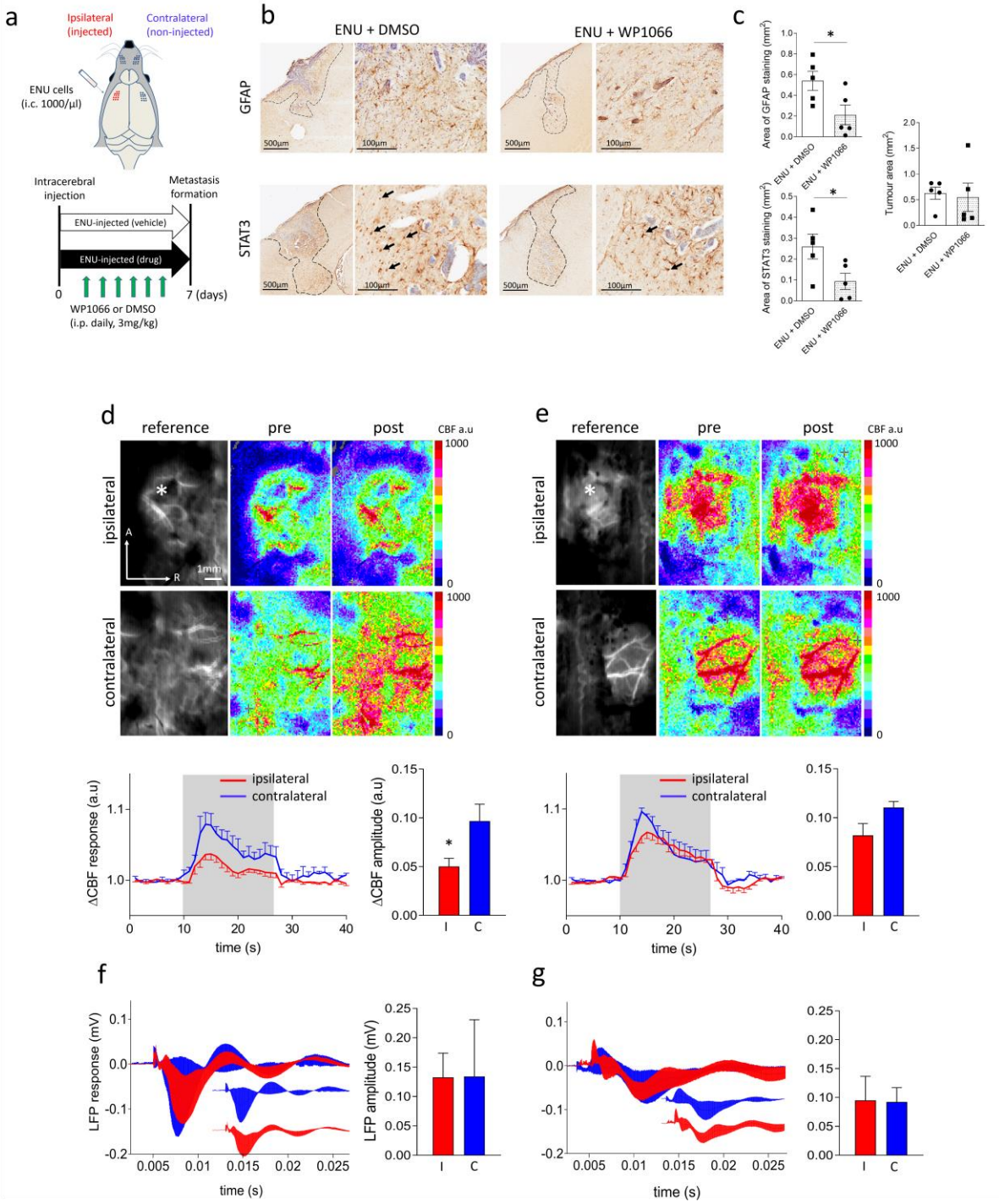
a
Ipsilateral (injected)
Contralateral (non-injected)
ENU cells (i.c. 1000/μl)
Intracerebral injection
Metastasis formation
ENU-injected (vehicle)
ENU-injected (drug)
0
7 (days)
WP1066 or DMSO (i.p. daily, 3mg/kg)
b
ENU + DMSO
ENU + WP1066
GFAP
STAT3
500μm
100μm
c
Area of GFAP staining (mm²)
Area of STAT3 staining (mm²)
Tumour area (mm²)
ENU + DMSO
ENU + WP1066
d
reference
pre
post
CBF a.u
1000
0
ipsilateral
contralateral
1mm
A
R
ΔCBF response (a.u)
time (s)
ΔCBF amplitude (a.u)
I
C
e
f
LFP response (mV)
LFP amplitude (mV)
g

Figure 4

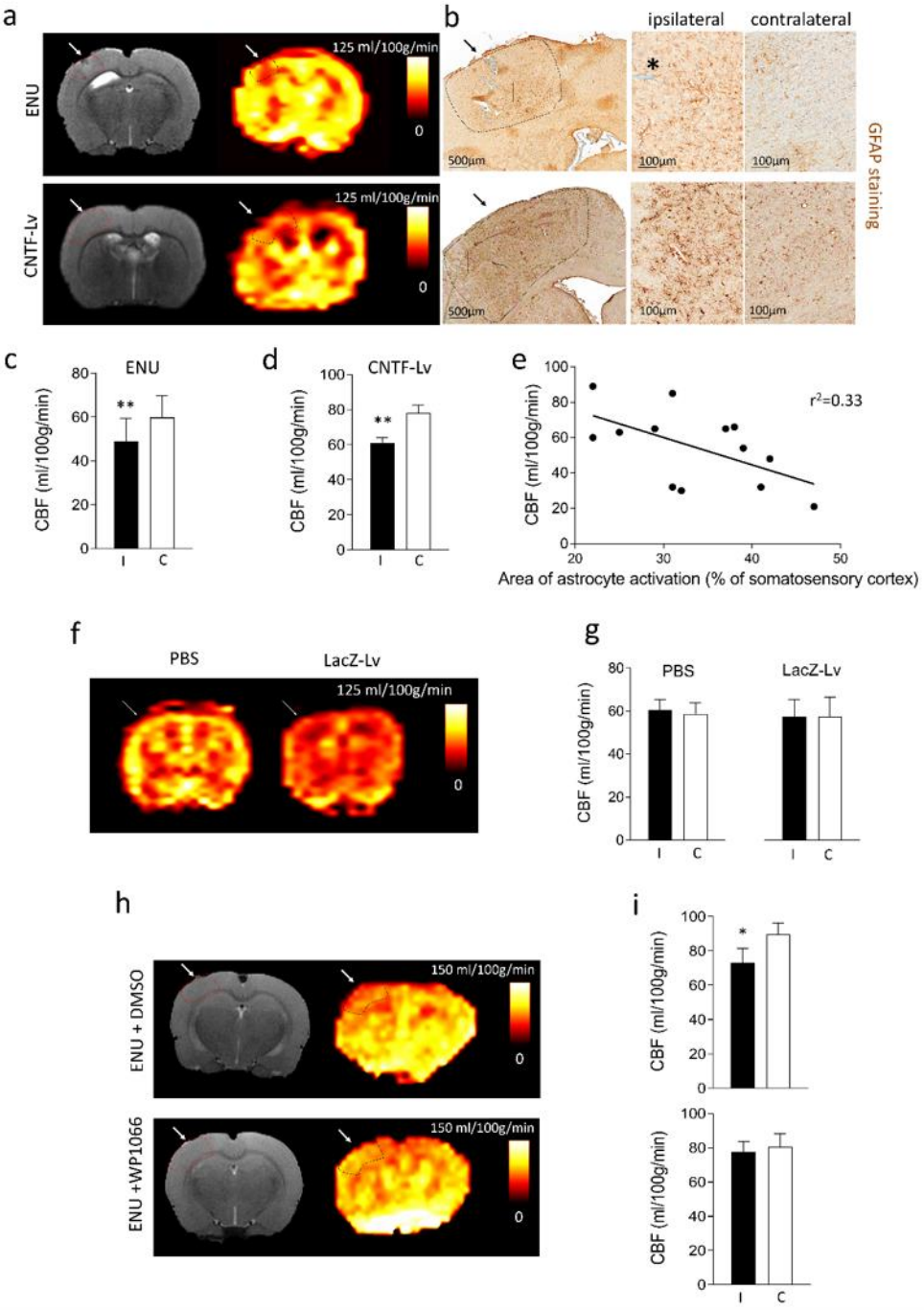
a
ENU
CNTF-Lv
125 ml/100g/min
0
b
ipsilateral
contralateral
GFAP staining
500µm
100µm
c
ENU
CBF (ml/100g/min)
**
I
C
d
CNTF-Lv
e
r²=0.33
Area of astrocyte activation (% of somatosensory cortex)
f
PBS
LacZ-Lv
g
h
ENU + DMSO
ENU +WP1066
150 ml/100g/min
i
*

Figure 5

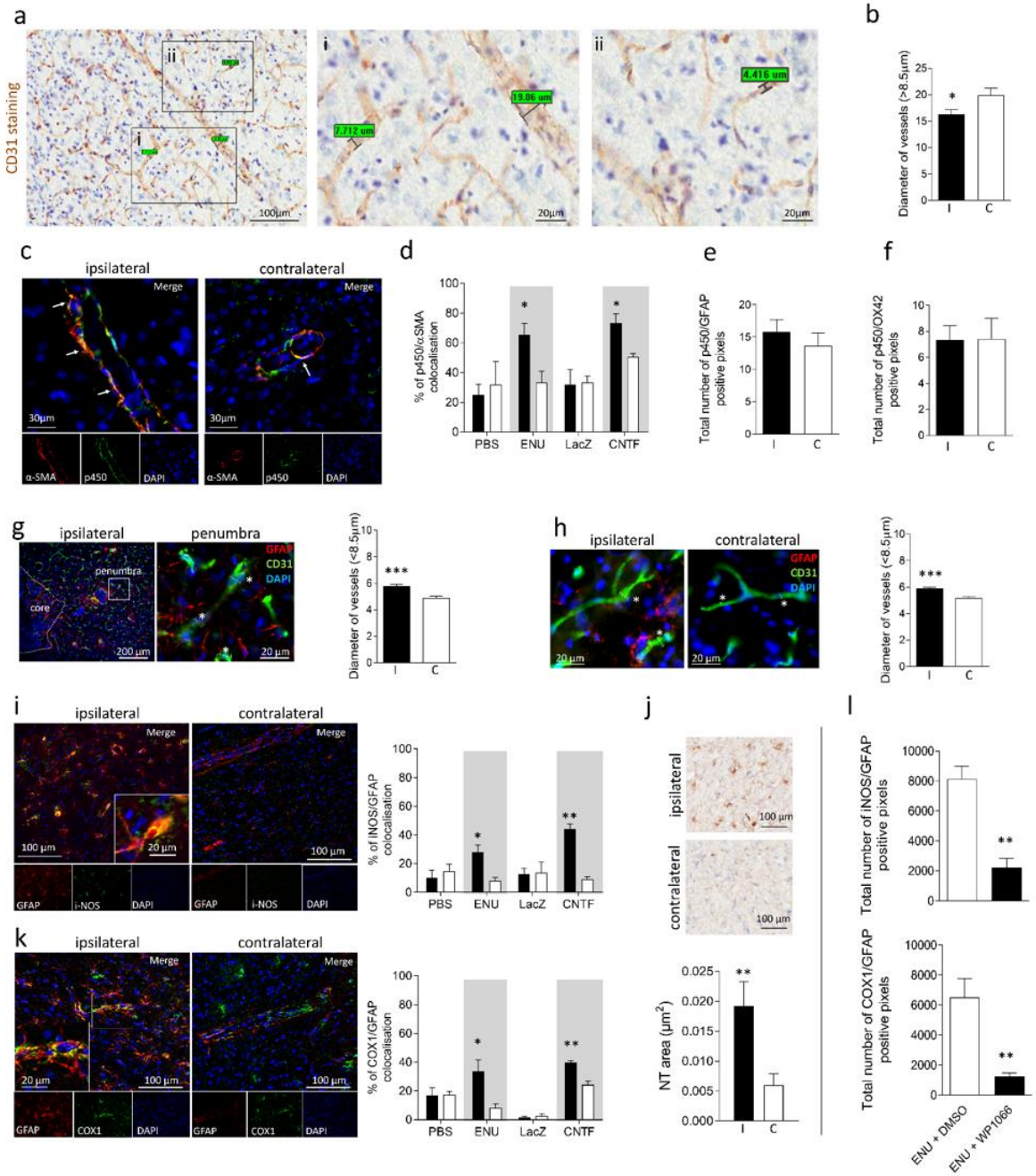
a
CD31 staining
ii
i
100µm
i
7.712 um
19.06 um
20µm
ii
4.416 um
20µm
b
Diameter of vessels (>8.5µm)
I
C
c
ipsilateral
contralateral
Merge
30µm
α-SMA
p450
DAPI
d
% of p450/αSMA colocalisation
PBS
ENU
LacZ
CNTF
e
Total number of p450/GFAP positive pixels
f
Total number of p450/OX42 positive pixels
g
ipsilateral
penumbra
core
200 µm
GFAP
CD31
DAPI
20 µm
Diameter of vessels (<8.5µm)
h
ipsilateral
contralateral
i
Merge
100 µm
20 µm
GFAP
i-NOS
DAPI
% of iNOS/GFAP colocalisation
j
ipsilateral
contralateral
100 µm
NT area (µm²)
k
COX1
% of COX1/GFAP colocalisation
l
Total number of iNOS/GFAP positive pixels
Total number of COX1/GFAP positive pixels
ENU + DMSO
ENU + WP1066

Figure 6

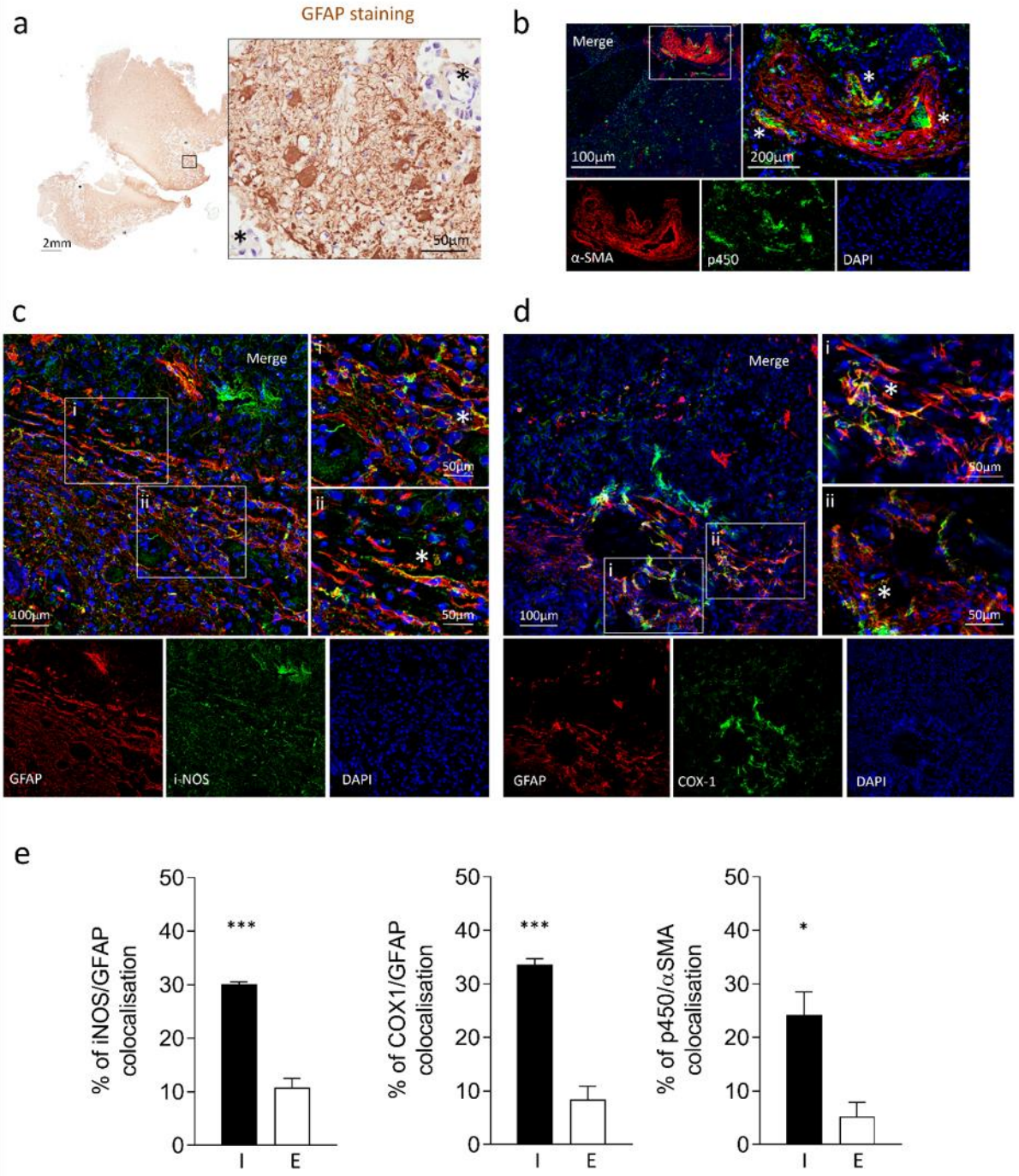
a
GFAP staining
2mm
50µm
b
Merge
100µm
200µm
α-SMA
p450
DAPI
c
Merge
i
ii
100µm
50µm
GFAP
i-NOS
DAPI
d
Merge
i
ii
100µm
50µm
GFAP
COX-1
DAPI
e
% of iNOS/GFAP colocalisation
% of COX1/GFAP colocalisation
% of p450/αSMA colocalisation
***
*
I
E